SIMULATION OF STRESS-STRAIN STATE OF Zr1.0%Nb ALLOY DURING EQUAL-CHANNEL ANGULAR PRESSING: PART 1. STRAIN DISTRIBUTION

H. ALSHEIKH[1], A. ROZHNOV[2], S. ROGACHEV[2], D. GRABCO[1,*], O. SHIKIMAKA[1]

[1] Institute of Applied Physics, State University of Moldova, Academy str., 5, Chisinau, 2028, Republic of Moldova
E-mails: hanan.alsheikh@ifa.usm.md; daria.grabco@ifa.usm.md; olga.shikimaka@ifa.usm.md
[2] National University of Science and Technology MISIS, Leninsky Prospekt, 4/1, Moscow, 119049, Russia
E-mails: aeforscc@yahoo.com; csaap@mail.ru
[*] *Corresponding author, E-mail*: daria.grabco@ifa.usm.md

Received August 21, 2024

Abstract: The simulation of a single pass of equal-channel angular pressing (ECAP) was conducted in the QFORM program. The strain distribution in the longitudinal and transverse sections of a Zr1.0%Nb alloy billet was calculated. This distribution was investigated at various moments (t_i, i = 1, 2, 3, 4) during the shearing deformation in the intersection channels (deformation zone).

Key words: zirconium alloy, ECAP, mathematical modeling.

DOI: https://doi.org/10.59277/RomJPhys.2024.69.617

1. INTRODUCTION

Regardless of the application area of zirconium alloys, be it nuclear power engineering [1–3] or medicine [4–8], the functional characteristics, such as corrosion resistance, physical and mechanical characteristics, and fatigue strength, plays an important role in their use. It is obvious that the higher the set of characteristics, the more widespread the alloy becomes. The latter circumstance leads to the need to search for ways to increase the level of functional characteristics and, first of all, physical and mechanical characteristics (tensile strength, yield strength, relative elongation at fracture, fatigue strength, and others). It has been proven that a significant increase in strength characteristics can be achieved by obtaining an ultra-fine-grained structure by using various methods of severe plastic deformation [9–17]. Severe plastic deformation is a process of material treatment using high strain. The process occurs with the formation of a non-porous, largely fragmented and disoriented structure. One of such methods is equal-channel angular pressing (ECAP) [18–20].

The development of computing power and the corresponding software based on the finite element method (ANSYS, QFORM, Deform, Multidef, etc.) initiated the solution of problems related to the substantiation of the theoretical foundations of various technological processes, in particular, issues related to the study of processes occurring during ECAP [21–25].

The aim of this work is to investigate the changes in the stress-strain state of Zr1.0%Nb alloy billet during ECAP. Studying the stress-strain state is essential for understanding deformation homogeneity across various sections during the shearing deformation in the channel intersection (deformation zone). Consequently, this investigation can be utilized to develop the optimal ECAP regime. The findings presented in this study focus on analyzing the strain distribution in the longitudinal and transverse sections of Zr1.0% Nb alloy billet during ECAP, using the 3-D finite element simulation method in the QFORM program.

2. MATERIALS AND METHODS

2.1. SIMULATION INPUTS

In this work, we simulated the ECAP process of Zr1.0%Nb alloy billet (110 mm long and 20 mm in diameter) for one single pass at 420ºC, although ECAP is experimentally carried out for six passes, following the B_C route, where the billet is rotated 90º in one direction around its longitudinal axis. The angle between the die channels is 108º. ECAP is carried out under isothermal conditions with a stepwise decrease in temperature as follows: 2 passes at T = 420ºC, 2 passes at T = 350ºC, and 2 passes at T = 300ºC. The deformation rate was 0.21 s^{-1}, with maximum pressing force of 0.3 mN and ram speed of 0.42 mm/s (25 mm/min).

The sequence of ECAP simulation in the QFORM software includes:

– entering the inputs data into the QFORM program;
– calculating the strain values in each node of the billet mesh;
– analyzing the simulation results.

The inputs data for the simulation encompasses:

– geometric parameters of the ECAP die and billet;
– physical and chemical characteristics of the ECAP die and billet.

2.2. GEOMETRICAL DIMENSIONS

The Compass 3D program is used to create the finite-element models of the ECAP instrument and the billet. Thus, three-dimensional finite-elements models of billet and ECAP instrument are constructed. These models include the billet, punch, and die. These three models are assembled as illustrated in (Fig. 1). The finite-elements mesh consists of 46,795 elements for the billet, and 55,693 elements for the ECAP instrument.

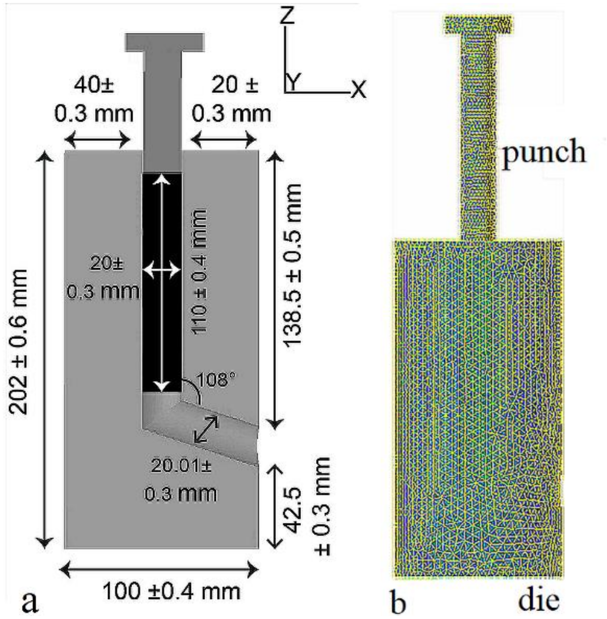

Fig. 1 – Dimensions of billet and die (a); assembled finite-element three-dimensional model of the ECAP instrument (b).

2.3. CHEMICAL AND PHYSICAL CHARACTERISTICS OF THE DIE AND BILLET

To run the simulation, it is necessary to input detailed information about the physical, chemical, and mechanical characteristics of both the billet and ECAP instrument into the QFORM program. Data on the Zr1.0%Nb alloy billet were obtained partially from reference books for physical properties, and partially through tensile and compression tests. The chemical composition of Zr1.0%Nb alloy is given in Table 1.

Table 1

Chemical composition of Zr1.0%Nb alloy

Element Contents [%]								
Nb	Fe	Ni	Al	Ti	C	Si	O	N
0.9-1.1	0.05	0.02	0.008	0.005	0.2	0.2	0.1	0.006

The samples for the various mechanical tests were taken from the as-received billet, which was manufactured at JSC Chepetsky Mechanical Plant (Russia).

The structure of the as-received billet was partially recrystallized. Mechanical tensile tests on the samples were performed at room temperature using an Instron 5966 testing machine with a testing speed of 1 mm/min.

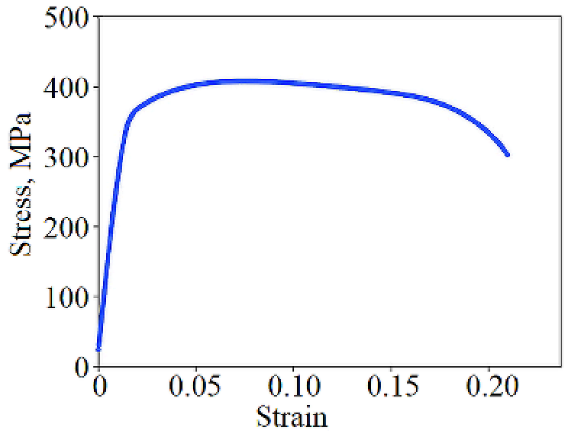

Fig. 2 – Stress-strain diagram of a Zr1.0%Nb alloy under tensile testing.

The samples were tested in their as-received state, which was partially recrystallized. A typical deformation diagram from the tensile test is shown in Fig. 2. The mechanical characteristics of the Zr1.0%Nb alloy were determined from the deformation diagrams of the tested samples: the average values of 0.2%-yield strength (YS), ultimate tensile strength (UTS), and relative elongation at fracture (RE) are given in Table 2.

Table 2

Mechanical characteristics of Zr1.0%Nb alloy under tensile test

YS [MPa]	UTS [MPa]	RE [%]
324 ± 5	420 ± 6	20.2 ± 2

Compression tests of Zr1.0%Nb alloy were conducted at different temperatures based on the experimental ECAP regime at 420, 350 and 300°C. Compression tests on various cylindrical samples were performed using the Gleeble System 3800 testing machine. A diameter of 7 mm and a height of 10 mm were selected for the cylindrical samples.

The samples were heated by an electric current to temperatures 420, 350 and 300°C, a thermocouple was attached to each sample to control the temperature. The resulting stress-strain diagrams of the Zr1.0%Nb alloy at these different temperatures are shown in Fig. 3.

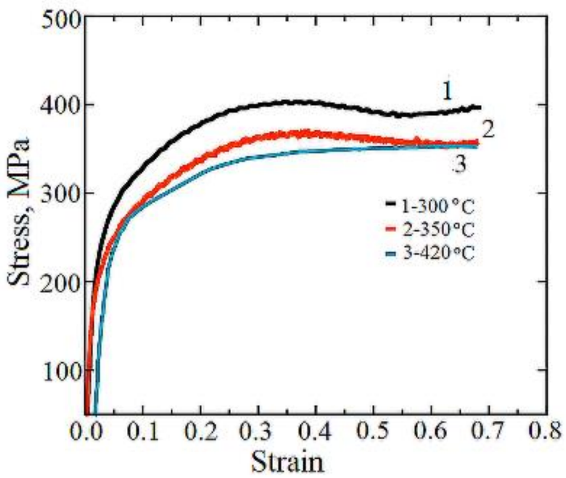

Fig. 3 – Stress-strain diagrams of Zr1.0%Nb alloy at various temperatures under compression testing.

The chemical composition and the physical characteristics of the ECAP instrument were selected from the QFORM database under category "High-strength alloy". The temperature of billet and ECAP instruments (die, and punch) during the simulation was set at $T = 420^{o}$C.

3. COMPUTATIONAL SIMULATION

General algorithm of ECAP simulation. QFORM program is capable of calculating the following values:

– sample temperature taking into account preliminary heating of the workpiece;
– strain;
– stress.

In this work, we investigate the strain distribution in the longitudinal (Z), (Y) and transverse sections in one single ECAP pass. The capabilities of the QFORM program allow calculations to be performed for any node of the billet mesh. To manage and minimize the amount of calculated data, some conditional approaches were utilized. These conditional approaches will be discussed in detail in the following paragraphs, which includes the investigated sections and their position at different stages of deformation.

Figure 4 illustrates the considered upper and lower surfaces of the billet, as well as its longitudinal Z and Y sections. Moreover, the surface of the billet passing through point O refers to the upper surface. Accordingly, the surface of the billet passing through point O_1 refers to the lower surface (Figs. 4a, b). Figures 4c and 4d illustrate the sections (Z) and (Y) respectively.

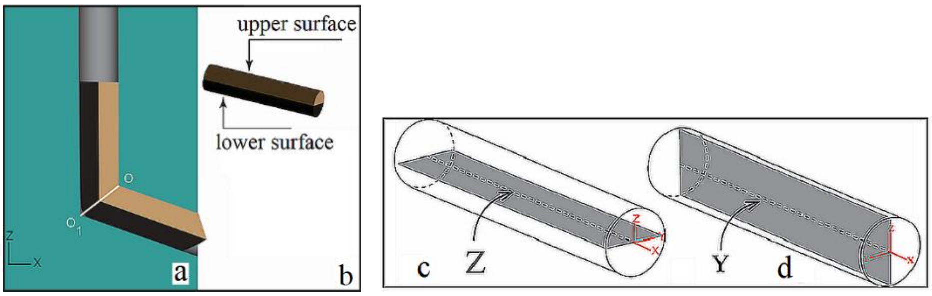

Fig. 4 – Upper and lower surfaces of billet (a, b), Z (c) and Y(d) longitudinal sections.

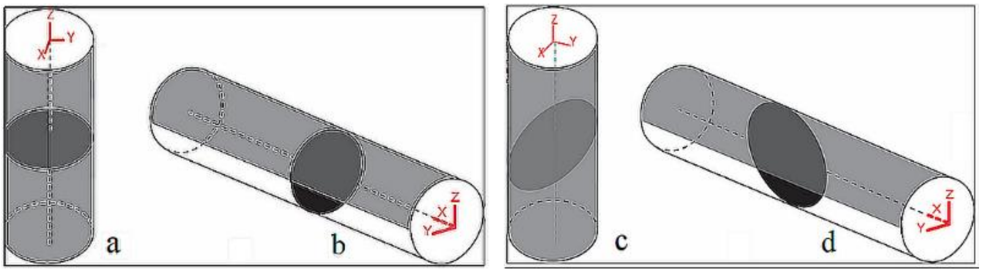

Fig. 5 – Transverse sections: a, b – circular sections; c, d – ellipsoidal sections.

The considered transverse sections (circular and ellipsoidal) are illustrated in Figs. 5a, c (top view) and Figs. 5b, d (front view).

The billet deformation moments or positions during its movement through the channels, specifically through the intersection channels zone, are selected as follows:

– moment t_1 represents the initial stage of deformation, where 25% of the billet length has traversed the deformation zone (intersection channels).
– moments t_2 and t_3 represent the intermediate stage of deformation, when 50 and 75% of the billet length, respectively, have traversed the deformation zone (intersection channels).
– moment t_4 represents the final stage of deformation, where 100% of the billet length has deformed completely, traversing the deformation zone.

These moments or stages of deformation, and the considered circular and ellipsoidal transverse sections are shown in Fig. 6. The position of these transverse sections was selected as follows:

– section (A) at a distance of 10 mm from the upper edge of the billet at t_1;
– section (B) at a distance of 5 mm from the deformation zone;
– section (C) in the deformation zone (intersection channels);
– section (D) at a distance of 5 mm beyond the deformation zone;
– section (E) at a distance of 10 mm from the extraction.

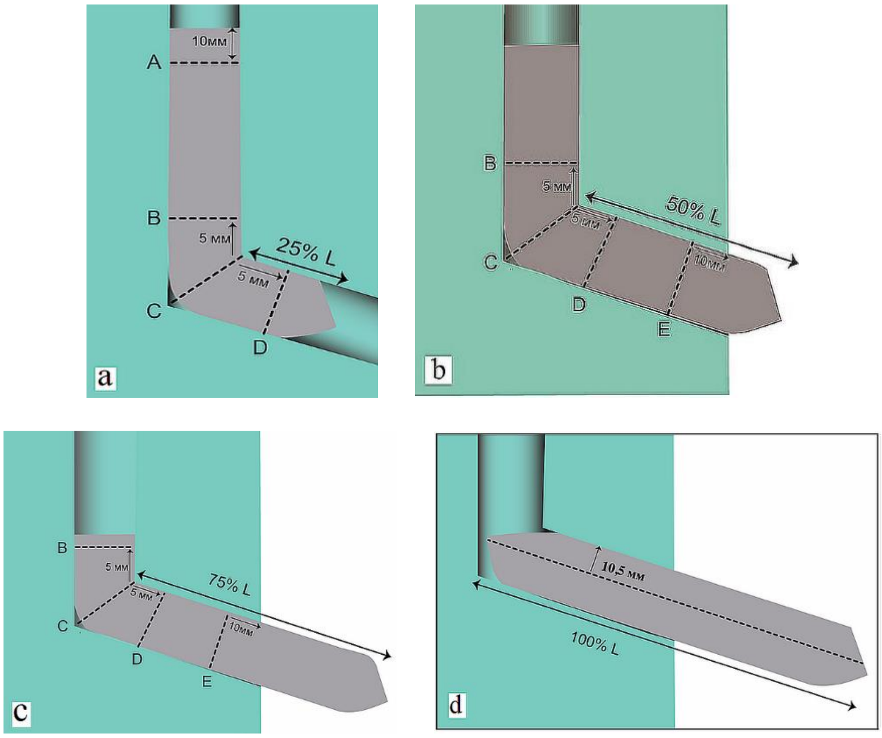

Fig. 6 – Deformation moments (stages) during ECAP: a – t_1; b – t_2; c – t_3 and d – t_4.

The position of the transverse sections is linked to the deformation stages or moments t_i, hence, Table 3 presents the considered circular and ellipsoidal transverse sections at different moments t_i during the billet deformation.

Table 3

Considered circular and ellipsoidal transverse sections of the billet at various moments t_i

Deformation moment (stages) t_i	Transverse Sections				
	Before deformation		Shearing deformation	After deformation	
	Circular sections		Ellipsoidal sections	Circular sections	
t_1	A(t_1)	B(t_1)	C(t_1)	D(t_1)	–
t_2	–	B(t_2)	C(t_2)	D(t_2)	E(t_2)
t_3	–	B(t_3)	C(t_3)	D(t_3)	E(t_3)
t_4	–	–	–	–	–

Thus, a total of nine circular transverse sections were obtained, four before the deformation zone and five after it. The area of these circular transverse sections varies between 306 and 312 mm^2. Three ellipsoidal transverse sections were obtained by inclining the cutting plane at an angle of 54º in the deformation zone, where the two channels intersect with equal diameters. These sections are marked as follows: C(t_1) at the initial stage, C(t_2) at the intermediate stage and C(t_3) at the final stage. The area of the ellipsoidal transverse sections varies between 340 and 350 mm^2. These transverse sections clearly detect the changes in the deformation plane within the shearing zone.

The area of the longitudinal sections at different moments of the ECAP deformation Y(t_1) (Fig. 6a), Y(t_2) (Fig. 6b), and Y(t_3) (Fig. 6c) fall within the range of 2200 to 2211 mm^2. At the final stage, the area of the longitudinal plane Y(t_4) is equal to 2301 mm^2. The horizontal position of the plane Y(t_4) (Fig. 6d) is achieved by rotating it counterclockwise by an angle of 18º.

4. RESULTS AND DISCUSSION

4.1. STRAIN DISTRIBUTION

Irreversible plastic deformations remain in the material after the removal of applied force. Thus, Fig. 7 shows the strain values (maximum, ε_{max}, minimum, ε_{min}, and average, ε_{av}), and their distribution at various moments along the longitudinal section $Y(t_i)$ (i = 1, 2, 3). It is evident that the calculated strain distribution exhibits a complex pattern, characterized by numerous sections with varying strain values. This correlates with the results of work [26], in which the effect of ECAP on the structure of the Zr1.0%Nb alloy was studied. It was shown that after ECAP, an extremely inhomogeneous ultrafine-grained microstructure is formed in the alloy, consisting of areas filled with cells and fragments with low misorientation and high dislocation density.

To quantify the inhomogeneity of the strain distribution across sections in Fig. 7, an inhomogeneity index C is used, which is defined as follows:

$$\mathrm{C} = \frac{\varepsilon_{max} - \varepsilon_{min}}{\varepsilon_{av}}$$

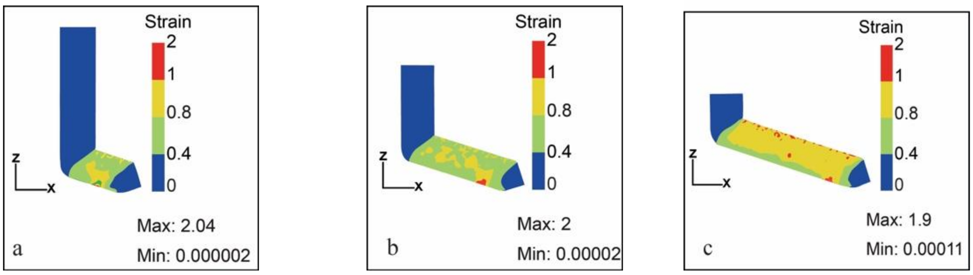

Fig. 7 – Strain distribution along longitudinal sections: a – Y(t_1), b – Y(t_2), c – Y(t_3).

The strain values along the billet after the first ECAP pass are conventionally divided into the following groups:

– group 1: high level of strain ($\varepsilon > 1$);
– group 2: moderate level of strain ($0.75 \leq \varepsilon \leq 1$);
– group 3: low level of strain ($0.35 \leq \varepsilon \leq 0.75$);
– group 4: very low level of strain ($0 \leq \varepsilon \leq 0.35$).

Figure 8 illustrates the distribution of strain groups across the longitudinal Y and Z sections after the completion of the ECAP deformation at moment (t_4).

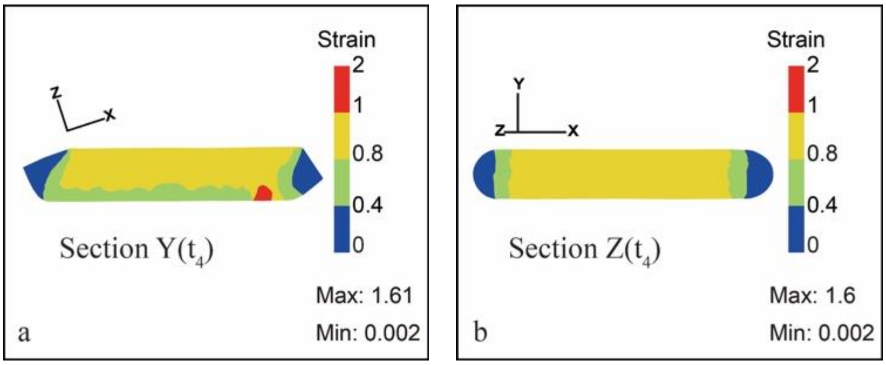

Fig. 8 – Strain distribution across sections: a – Y(t_4), b – Z(t_4).

It is obvious from Fig. 8 that the strain along the billet is non-uniform. Specifically, the strain values on the lower surface, after passing the corner of the die, is smaller (indicated by the green area) compared to the strain values on the upper surface, and middle zone of the billet.

Table 4 presents the values of the areas % occupied by the different strain groups on the longitudinal sections Y(t_1), Y(t_2), Y(t_3) and Y(t_4). Table 5 presents the calculated values of the inhomogeneity indexes C_1, and C_2. Index C_1 encompasses all strain values, including those in group 4. In contrast, C_2 excludes the strain values in group 4, which refers to the undeformed billet in the entry channel.

Table 4

Area % of related strain groups

Strain Group	Strain value ε	Longitudinal Sections Y(t_i)			
		Y(t_1)	Y(t_2)	Y(t_3)	Y(t_4)
1	$\varepsilon > 1$	0.5	0.6	0.7	1.2
2	$0.75 \leq \varepsilon \leq 1$	10	28	45	53
3	$0.35 \leq \varepsilon \leq 0.75$	14	21	29	33
4	$0 \leq \varepsilon \leq 0.35$	75	50	26	12

Table 5

Inhomogeneity indexes on longitudinal sections

Inhomogeneity Index C	Longitudinal Sections			
	$Y(t_1)$	$Y(t_2)$	$Y(t_3)$	$Y(t_4)$
C_1	5	3.5	2.7	2.3
C_2	2	3.2	1.9	1.7

In the entry channel, the stress-strain values are distributed uniformly. In this channel, only the area occupied by strain group (4) (undeformed zones) changes during the ECAP process. As shown in Table 4, after the first ECAP pass, the area occupied by strain group 4 decreases gradually. Conversely, the area occupied by the strain groups (1, 2, and 3) increases, reflecting the deformation of the billet as it moves through the deformation zone. Consequently, the inhomogeneity index C_2 decreases, indicating a more uniform strain distribution.

Strain distribution on the transverse sections of the billet reveals that, before entering the deformation zone, the material in the entry channel remains almost undeformed, the strain on the section $A(t_1)$ is very low (Fig. 9). The maximum strain values on the upper and lower surfaces vary from 0.0001 to 0.002. Similarly, low strain values are observed in sections $B(t_1)$, $B(t_2)$ and $B(t_3)$ (Fig. 10). Strain values up to 0.0005 occupy 91% and 93% of the area of sections $B(t_1)$ and $B(t_2)$ respectively. In section $B(t_3)$, the area with these low strain decreases to 58% due to increase strain on the upper and lower surfaces. This indicates that the billet deforms more intensely on the upper and lower surfaces compared to the central zone.

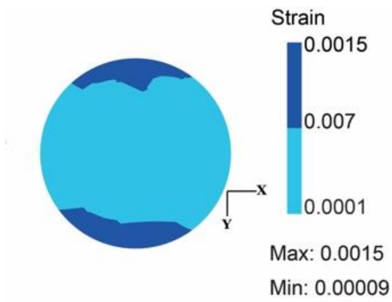

Fig. 9 – Strain distribution in section $A(t_1)$.

In the shearing zone, strain begins to increase on the ellipsoid sections with a maximum strain value of 0.4 detected (Fig. 11). The central zone with a high strain ($\varepsilon > 0.28$) is located between two zones with low strain ($\varepsilon < 0.28$) on the upper and lower surfaces of the section. The area of the central zone increases from 60% in the section $C(t_1)$ to a maximum of 78% in section $C(t_2)$. However, this area decreases to

45% in the section C(t_3) as the proportion of the section area occupied by zones with low strain changes. Notably, that the strain distribution in section C(t_2) indicates an increase in the homogeneity of the strain distribution.

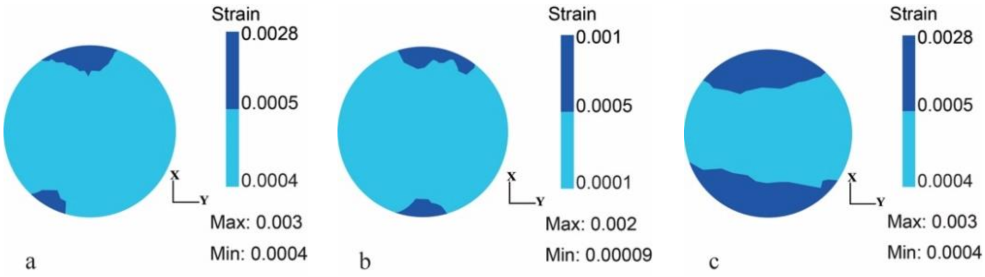

Fig. 10 – Strain distribution in sections: a – B(t_1), b – B(t_2), c – B(t_3).

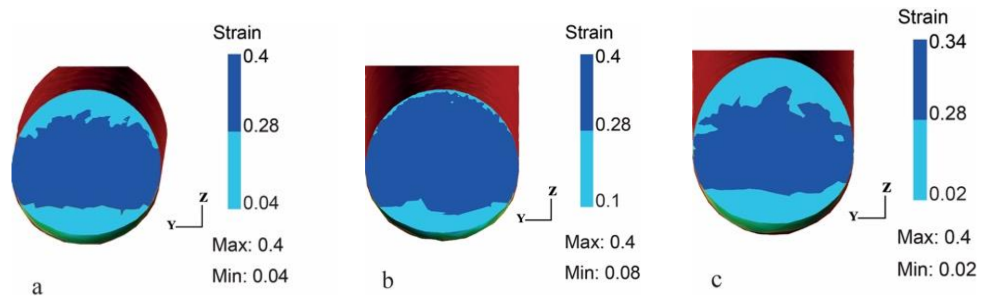

Fig. 11 – Strain distribution in sections: a – C(t_1), b – C(t_2), c – C(t_3).

In general, after passing the deformation zone, a zone with high strain ($1 < \varepsilon \leq 1.2$) appears on the section D(t_1), which occupies a small area of 1.7% relative to the entire cross-section area. Additionally, a slightly lower level of strain ($0.75 < \varepsilon \leq 1$) is detected in a zone that occupies 95% of the cross-sectional area of D(t_1) (Fig. 12).

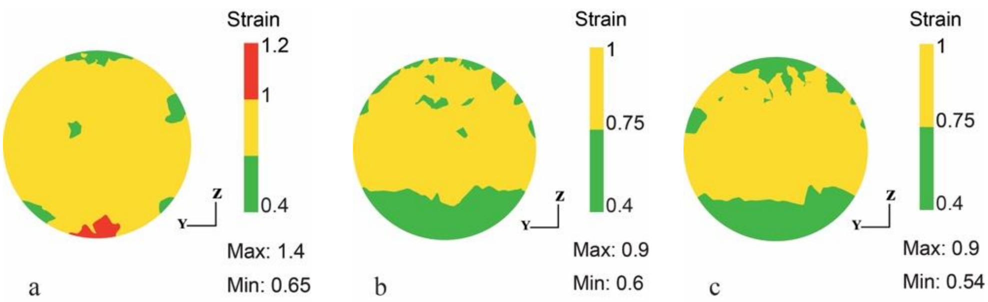

Fig. 12 – Strain distribution in sections: a – D(t_1), b – D(t_2), c – D(t_3).

In sections D(t_2) and D(t_3) this zone ($0.75 < \varepsilon \leq 1$) occupies almost the same area (79 and 78%, respectively). These zones are localized in the center of the transverse sections. The low strain zones ($0.4 < \varepsilon \leq 0.75$) are found on the upper and lower surfaces of these sections. Section D(t_1) has the highest inhomogeneity index (0.8) compared to sections D(t_2) and D(t_3), where the index is lower, at 0.4.
The strain distribution in the sections E(t_2) and E(t_3) is illustrated in Fig. 13. The strain values fall into two zones. The high-strain zone (from 0.75 to 1) occupies 91% of the area in section E(t_2) and 79% of the area in section E(t_3).

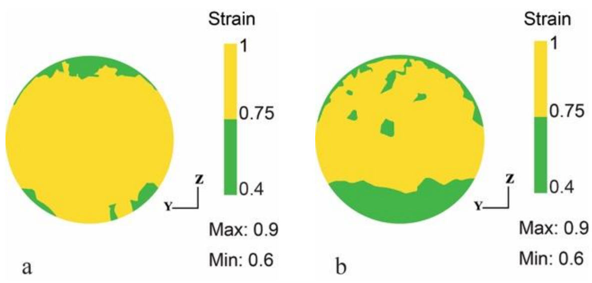

Fig. 13 – Strain distribution in sections: a – E(t_2), b – E(t_3).

In section E(t_2), the low-strain zone ($0.4 < \varepsilon \leq 0.75$) predominantly occupies the upper surface, with smaller areas on the lower surface. In contrast, in section E(t_3) the low-strain zone is more extensive on the lower surface, with smaller areas near the upper surface.

It is known from the literature [27, 28] that changes in the crystal structure of the sample significantly affect the hardness value, at the same time a decrease in the grain size to micro- and nano-sizes is accompanied by an increase in micro- and nano-hardness. Therefore, the hardness value can be a parameter that reflects a change in the crystal structure. Thus, in the work [29] an increase and non-uniform distribution of hardness was obtained in Al-6061 samples subjected to ECAP, which may indicate non-uniform distribution of the newly created grain structure. Other authors [30] found that the greatest increase in microhardness occurs in the upper and central parts of the billet cross-section, and a lower increase is noted on the lower surface. This correlates with the results obtained in our article, that the low-strain zone occurs on the lower surface, while the high-strain zone is observed in the central and upper surfaces of the cross-section of the sample.

5. CONCLUSIONS

The QFORM software was provided a computational simulation of stress-strain state of a cylindrical billet from Zr1.0%Nb alloy during ECAP for one single pass. Strain distributions on the longitudinal and transverse sections at various moments of ECAP deformation at a temperature of 420°C are obtained. This distribution reveal inhomogeneity in deformation through ECAP. It was found that the calculated distribution of deformations has a complex pattern, characterized by numerous areas with changing deformation values.

This deformation inhomogeneity gradually decreases along the longitudinal section. By the final stage of deformation, the inhomogeneity index decreased. In the shearing zone (intersection channels), the strain distribution is quite uniform. The central zone of the ellipsoidal section, where maximum deformation is detected, occupies almost the total area of the section.

Acknowledgements. This study was supported by the research Subprogram **011201** of the Institute of Applied Physics, State University of Moldova, funded by the Ministry of Education and Scientific Research of Moldova Republic.

REFERENCES

1. H. M. Ghadeer, K. Karuppasamy, M. Alrwashdeh, I. Barsoum, S. Alameri, and A. Alfantazi, Alexandria Eng. J. **108**, 13–39 (2024).
2. J. Guanyu, X. Donghai, Y. L. L. Wanpeng, Z. Youwei, and Y. Jianqiao, Progress in Nuclear Energy **154**, 104490 (2022).
3. Y. Suresh, G. Anand, In *Structural Alloys for Nuclear Energy Applications,* Odette, R.G., Zinkle, S.J. (Eds.), Elsevier, Amsterdam **247–291** (2019).
4. X. Chaoqun, Z. Na, C. Bohan, M. Jingwei, S. Tianshuo, W. Xinyu, Y. Tai, Z. Xinyu, and L. Qiang, MSEA **900**, 146486 (2024).
5. X. Xiaoning, S. Xiaohui, T. Yueyan, Z. Ligang, and L. Libin, Mat. Character **205**, 113356 (2023).
6. C. Divya, G. Tianqi, G. Karan, and I. Sašo, Dental Materials **40**(1), 1–17 (2024).
7. L. Saldaña, L. Jiang, M. Multigner, *et al.*, Biomaterials **28**, 4343–4354 (2007).
8. T. Zhang, P. Ou, J. Ruan, H. Yang, J. Biomater. Appl. **35**(10), 1284–1293 (2021).
9. S.A. Nikulin, A.B. Rozhnov, S.O. Rogachev, V.M. Khatkevich, V.A. Turchenko, and E.S. Khotulev, Mater. Lett. **169**, 223–226 (2016).
10. Y. Sharkeev, A. Eroshenko, E. Legostaeva, Z. Kovalevskaya, O. Belyavskaya, M. Khimich, M. Epple, O. Prymak, V. Sokolova, Q. Zhu, *et al.*, Metals **12**, 1136 (2022).
11. V. Sklenicka, J. Dvorak, P. Kral, I.V. Betekhtin, G.A. Kadomtsev, V.M. Narykova, V.S. Dobatkin, K. Kucharova, and M. Kvapilova, Mater. Sci. Eng. A **820**, 141570 (2021).
12. M.V.P. Companhoni, J.R.G. Matheus, T.L. Marcondes, and A.L.J. Pinto, Mat. Sci. **47**(22), 7835–7840 (2012).
13. R. Haraguchi, Y. Yoshimatsu, T. Nagaoka, M. Arita, K. Edalati, and Z.J. Horita, Mat. Sci. **52**, 6778–6788 (2017).
14. A.P. Zhilyaev, I. Sabirov, G. González-Doncel, J. Molina-Aldareguía, B. Srinivasarao, and M.T. Pérez-Prado, Mater. Sci. Eng. A **528**, 3496–3505 (2011).
15. V. Sklenicka, J. Dvorak, P. Kral, M. Svoboda, M. Kvapilova, V.I. Kopylov, S.A. Nikulin, and S.V. Dobatkin, Acta Physica Polonica A **122**(3), 485–489 (2012).
16. B.S. Lee, M.H. Kim, S.K. Hwang, S.I. Kwun, S.W. Chae, Mater. Sci. Eng. A **449–451**, 1087–1089 (2007).
17. S.O. Rogachev, A.B. Rozhnov, S.A. Nikulin, O.V. Rybalchenko, M.V. Gorshenkov, V.G. Chjen, and S.V. Dobatkin, Phys. Met. Metallogr. **117**(4), 371–377 (2016).

18. N. Sadasivan, M. Balasubramanian, B.R. Rameshbapu, J. Manuf. Process. **59**, 698–726 (2020).
19. L. Cui, S. Shao, H. Wang, G. Zhang, Z. Zhao, S. Zhao, Processes **10**, 2181 (2022).
20. P.I. Semenova, Z.R. Valiev, G.T. Langdon, and H. Garbacz. P.I. Semenova, S. Zherebtsov, M. Zherebtsov (Eds.), Elsevier, Amsterdam, 3–19, 2019.
21. A.E. Sosenushkin, A.E. Artek, E.N. Sosenushkin, Mechanical Engineering Technology **12**, 53–56 (2011) (in Ru.).
22. A. Ghosh, M. Ghosh, Mater. Today Commun. **26**, 102112 (2021).
23. M.K. Agarwal, A. Singhal, A. Kapoor, D. Bhatia, Materials Science for Energy Technologies **4**, 290–295 (2021).
24. V. dos A. Costa, K.F.D.S. Ramos, W.W. Batista, E. de O. Santos, Research, Society and Development **11**(15), 37139 (2022).
25. J. Wongsa-Ngam, N. Noraphaiphipaksa, C. Kanchanomai, T.G. Langdon, Crystals **11**, 1505 2021).
26. A.B. Rozhnov, S.O. Rogachev, Khanan Alsheikh, and D.V. Prosvirnin. Phys. Met. Metallogr. **123**(1), 99–105 (2022).
27. Yu.I. Golovin. Phys. Sol. State **50**(12), 2113–2142 (2008).
28. Yu.S. Boyarskaya. D.Z. Grabco, M.S. Kats, *Physics of Microindentation Processes*. Chisinau, Stiinta, 1986.
29. Ch. Xu, M. Furukawa, Z. Horita, T.G. Langdon. Mater. Sci. Eng. A **398**, 66–76 (2005).
30. M. Prell, Ch. Xu, T.G. Langdon. Mater. Sci. Eng. A **480**, 449–455 (2008).